J. Appl. Comput. Mech., 6(SI) (2020) 1335-1347
DOI: 10.22055/JACM.2020.34192.2353

ISSN: 2383-4536
jacm.scu.ac.ir

Shahid Chamran University of Ahvaz

Journal of Applied and Computational Mechanics

Research Paper

An 8-Node Solid-Shell Finite Element based on Assumed Bending Strains and Cell-Based Smoothed Membrane Strains for Static Analysis of Plates and Shells

Thanh Chau-Dinh[1], Nhat Le-Tran[2]

[1] Faculty of Civil Engineering, Ho Chi Minh City University of Technology and Education, 01 Vo Van Ngan Street, Thu Duc District, Ho Chi Minh City, Vietnam, Email: chdthanh@hcmute.edu.vn

[2] Aurecon Vietnam Co., 72-74 Nguyen Thi Minh Khai Street, District 3, Ho Chi Minh City, Vietnam, Email: trannhat93@gmail.com

Received June 29 2020; Revised August 03 2020; Accepted for publication August 05 2020.
Corresponding author: T. Chau-Dinh (chdthanh@hcmute.edu.vn)

Abstract. In this paper, a new 8-node solid-shell finite element is proposed. The transverse shear strains and transverse normal strains of the element are separately interpolated and related to the C^0-displacement approximation at tying points to overcome the shear- and trapezoidal-locking phenomena. From the bending strain approximation suggested for degenerated shell elements, the assumed bending strains for the solid-shell element are firstly established. The membrane strains of the element are smoothed on domains defined by dividing the middle surface's element into 1, 2, 3 or 4 sub-cells in accordance with the cell-based strain smoothing (CS) technique. The formulations of the membrane stiffness matrices are explicitly integrated on the boundary lines of the smoothing sub-cells. The proposed CSn-Q8 element, in which n is the number of smoothing sub-cells, is verified through static analysis of several benchmark plate and shell problems. Numerical results show the improved performance of the CSn-Q8 element in comparison with other references.

Keywords: plates and shells, 8-node solid-shell element, assumed bending strains, cell-based smoothed membrane strains.

1. Introduction

Plates and shells are some of the most suitable choices for structures which require the highest safety, convenience, and aesthetics. In fact, the plate and shell structures are popularly used in such many industries as civil, aerospace, shipping, and automobile engineering. Therefore, accurate computation of the plate and shells' behaviors is necessary.

Among many numerical methods that have been developed to solve the plate and shell structures, the finite element method (FEM) is the most popular and effective. The formulations of plate and shell finite elements are usually established by using the first-order shear deformation theory combined with locking-removal techniques to eliminate exaggerated strains. These plate and shell finite elements employ C^0 continuous approximations of displacements and can analyze both thin and thick plate and shell structures. According to this approach, the formulations of plate and shell finite elements can be divided into 3 kinds: (1) flat shell, (2) degenerated continuum mechanics shell, and (3) solid-shell finite elements [1]. The flat shell and degenerated continuum mechanics shell finite elements predict the plates and shells' behaviors on their middle surfaces and require rotational displacements besides translational ones. Because of pure combination of membrane and plate finite elements, the flat shell finite elements cannot describe the interaction between the membrane and bending behaviors. To overcome this shortcoming, the degenerated continuum mechanics shell finite elements are constructed from the 3-dimensional elastic deformation theory constrained by zero normal strains in the directions perpendicular to the middle surfaces of the elements. In contrast, the formulations of the solid-shell finite elements are completely derived from the 3-dimensional elastic deformation theory and consider changes of the strains through the shells' thickness. As a result, the solid-shell finite elements only have translational displacements and can be easily combined with other types of finite elements.

Using displacement approximations based on the C^0 shape functions, 8-node solid-shell elements are the simplest ones. However, the transverse shear strains of the elements purely derived from the C^0 displacement approximations cannot reduce to zero and lead to the shear-locking phenomenon when employed to analyze thin plates and shells. To attenuate the shear-locking phenomenon, the transverse shear strain fields are separately interpolated and connected to the displacement approximations at tying points. According to these approaches, many shear-locking removal techniques have been successfully developed such as the assumed natural strains (ANS) [2], enhanced assumed strains (EAS) [3], or mixed interpolation tensorial components (MITC) [4]. Furthermore, when largely curved shells are discretized by the 8-node solid-shell elements, the trapezoidal shapes of the elements cause additional normal strains in the thickness direction of the shells. This phenomenon is named the trapezoidal locking. Similar to the shear-locking removal techniques, the trapezoidal-locking phenomenon is also eliminated by interpolating the transverse normal strains through their values derived from the C^0 displacement approximation at tying points [5]. The 8-

Published online: August 28 2020

node solid-shell elements which employ the shear- and trapezoidal-locking removal techniques have managed geometrically linear and nonlinear analyses of plate and shell structures [5–9].

In an effort to improve the convergence rate of 4-node quadrilateral degenerated shell finite elements, Choi and Paik [10] have proposed the approximations of the membrane strains from only translational displacements of nodes located on the middle surfaces. To the solid-shell elements, the displacements are approximated from the translational displacements of nodes located on the elements' top and bottom surfaces, and the membrane and bending strains are obtained by derivatives of the displacement approximations. Then, Choi and Paik's technique can be modified to interpolate the membrane and bending strains of the solid-shell elements. However, in the study of 6-node solid-shell elements, the membrane approximations based on the Choi and Paik's suggestion are not effective because of low accuracy [11]. Therefore, in this work, Choi and Paik's technique was applied to the bending strain approximations of the solid-shell elements to enhance bending behaviors of the plate and shell structures.

Recently, the smoothed-FEM (S-FEM) [12] have been introduced to reduce the differences in strain fields between elements in discretized bodies. Such techniques based on edge-based (ES-), node-based (NS-), or cell-based (CS-) smoothing domains have been developed for plate and flat shell finite elements like MITC4, MITC3, DGS3, MIN3 ones. Numerical results show that owing to the smoothed strains, the accuracy and convergences of these elements are improved [13–18]. However, there are very few studies of applying the smoothing techniques to the solid-shell finite elements. Particularly, both membrane and bending strains in the resultant 8-node solid-shell finite elements have been smoothed on cell-based domains for geometrical linear analysis [19], or the 6-node solid-shell elements have stiffness matrix determined on the edge-based smoothing domains for laminated shell structures [20].

As a result, a novel 8-node solid-shell finite element was proposed in this paper. Besides the conventional techniques to remove the shear- and trapezoidal-locking phenomena, the presented element had the bending strains independently interpolated and the membrane strains smoothed on cell-based domains. By using the divergence theorem, the membrane stiffness matrices were explicitly integrated on the boundary lines of the smoothing domains. The presented element is called the cell-based smoothed 8-node solid-shell finite element, or CSn-S8 element in which *n* = 1, 2, 3, 4 are number of sub-cell domains used in the element.

In the next section, the formulation of the proposed solid-shell element is presented in detail. The convergence rate and accuracy of the presented element were evaluated by comparing with other reference elements in several benchmark plate and shell problems in Section 3. In the last section, some conclusions are drawn.

2. A Cell-based Smoothed 8-node Solid-Shell Finite Element (CSn-S8)

Consider a shell structure like a roof which is discretized by 8-node solid-shell elements as shown in **Fig. 1**. In the global Cartesian coordinate system OXYZ, coordinates $\mathbf{X}(X,Y,Z)$ of a point located in the solid-shell element can be determined by [6]

$$\mathbf{X} = \bar{\mathbf{X}} + t\mathbf{P} \tag{1}$$

in which, $\bar{\mathbf{X}}$ is the coordinates of a point on the middle surface, $\mathbf{P}$ is half of the vector connecting the bottom surface to the top one of the element, and *t* is the axis normal to the middle surface of the parent coordinate system *rst* attached to the element.

The coordinates $\bar{\mathbf{X}}$ and $\mathbf{P}$ are approximated by

$$\bar{\mathbf{X}} = \sum_{I=1}^{4} N_I \bar{\mathbf{X}}_I;\ \mathbf{P} = \sum_{I=1}^{4} N_I \mathbf{P}_I \tag{2}$$

with

$$N_1 = 0.25(1-r)(1-s);\ N_2 = 0.25(1+r)(1-s);\ N_3 = 0.25(1+r)(1+s);\ N_4 = 0.25(1-r)(1+s) \tag{3}$$

$$\bar{\mathbf{X}}_I = [X_I\ Y_I\ Z_I] = \frac{1}{2}\left(\mathbf{X}_I^t + \mathbf{X}_I^b\right);\ \mathbf{P}_I = [P_{XI}\ P_{YI}\ P_{ZI}] = \frac{1}{2}\left(\mathbf{X}_I^t - \mathbf{X}_I^b\right) \tag{4}$$

where, $\mathbf{X}_I^t$ and $\mathbf{X}_I^b$ are respectively the nodal coordinates of the element's top and bottom surfaces as defined in **Fig. 1**.

From eq. (2), the coordinates $\mathbf{X}$ in eq. (1) can be rewritten

$$\mathbf{X} = \sum_{I=1}^{4} N_I\left(\bar{\mathbf{X}}_I + t\mathbf{P}_I\right) \tag{5}$$

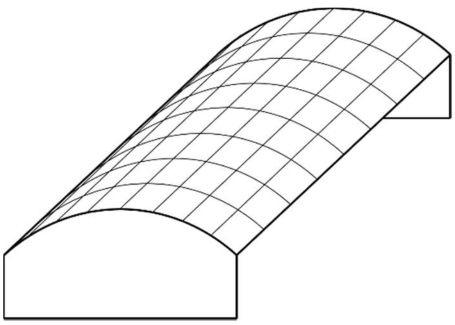

(a)

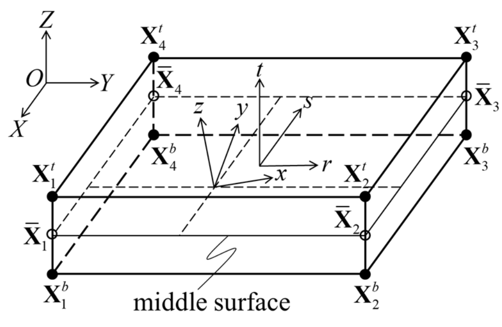

(b)

Fig. 1. (a) Schematic configuration of the shell structure and (b) Definition of geometry and coordinates of an 8-node solid-shell element.

For convenience, a local coordinate system *oxyz* for each element is constructed from unit base vectors defined by

$$\mathbf{R}_z = \frac{\mathbf{R}_r \times \mathbf{R}_s}{|\mathbf{R}_r \times \mathbf{R}_s|}; \mathbf{R}_x = \frac{\mathbf{R}_r}{|\mathbf{R}_r|}; \ \mathbf{R}_y = \mathbf{R}_z \times \mathbf{R}_x \tag{6}$$

in which,

$$\mathbf{R}_r = \mathbf{X}_{,r}\big|_{t=0} = \sum_{I=1}^{4} N_{I,r}\bar{\mathbf{X}}_i; \ \mathbf{R}_s = \mathbf{X}_{,s}\big|_{t=0} = \sum_{I=1}^{4} N_{I,s}\bar{\mathbf{X}}_i \tag{7}$$

Note that in this paper, the derivative of a function with respect to a variable is denoted by a subscript comma.
In the local coordinate system *oxyz* of the element, the displacements $\mathbf{u} = [u_X \ u_Y \ u_Z]^T$ are determined by [6]

$$\mathbf{u} = \bar{\mathbf{u}} + t\mathbf{p} \tag{8}$$

herein, $\bar{\mathbf{u}} = [\bar{u}_X \ \bar{u}_Y \ \bar{u}_Z]^T$ is the displacements of the middle surface, and $\mathbf{p}$ is half of the vector connecting the displacements of the bottom nodes to the top ones.
The displacements $\bar{\mathbf{u}}$ and $\mathbf{p}$ are approximated by

$$\bar{\mathbf{u}} = \sum_{I=1}^{4} N_I \bar{\mathbf{u}}_I; \ \mathbf{p} = \sum_{I=1}^{4} N_I \mathbf{p}_I \tag{9}$$

with

$$\bar{\mathbf{u}}_I = [\bar{u}_{XI} \ \bar{u}_{YI} \ \bar{u}_{ZI}]^T = \frac{1}{2}\left(\mathbf{u}_I^t + \mathbf{u}_I^b\right); \ \mathbf{p}_I = [p_{XI} \ p_{YI} \ p_{ZI}]^T = \frac{1}{2}\left(\mathbf{u}_I^t - \mathbf{u}_I^b\right) \tag{10}$$

in which, $\mathbf{u}_I^t$ and $\mathbf{u}_I^b$ are respectively the nodal displacements of the top and bottom surfaces in the local coordinate system.
Substituting eq. (9) into eq. (8), the displacements are expressed by

$$\mathbf{u} = \sum_{I=1}^{4} N_I \left(\bar{\mathbf{u}}_I + t\mathbf{p}_I\right) \tag{11}$$

The relations of the coordinates and displacements between the local and global coordinate systems and vice versa are

$$\mathbf{x} = \mathbf{R}^T\mathbf{X}; \ \mathbf{X} = \mathbf{R}\mathbf{x}; \ \mathbf{u} = \mathbf{R}^T\mathbf{U}; \ \mathbf{U} = \mathbf{R}\mathbf{u} \tag{12}$$

herein, $\mathbf{R} = [\mathbf{R}_x \ \mathbf{R}_y \ \mathbf{R}_z]$ is the transformation matrix.
From the displacement fields in eq. (8), the strain fields in the local coordinate system are determined by

$$\boldsymbol{\varepsilon} = \left[\varepsilon_{xx} \ \varepsilon_{yy} \ \gamma_{xy} \ \varepsilon_{zz} \ \gamma_{xz} \ \gamma_{yz}\right]^T = \begin{Bmatrix} \boldsymbol{\varepsilon}_m + t\boldsymbol{\varepsilon}_b \\ \varepsilon_{zz} \\ \boldsymbol{\varepsilon}_s \end{Bmatrix} \tag{13}$$

where, $\boldsymbol{\varepsilon}_m$, $\boldsymbol{\varepsilon}_b$, $\boldsymbol{\varepsilon}_s$, ε_{zz} are respectively the membrane, bending, transverse shear and transverse normal strains defined as

$$\boldsymbol{\varepsilon}_m = \left[\bar{u}_{x,x} \ \bar{u}_{y,y} \ \bar{u}_{x,y} + \bar{u}_{y,x}\right]^T; \ \boldsymbol{\varepsilon}_b = \left[p_{x,x} \ p_{y,y} \ p_{x,y} + p_{y,x}\right]^T; \ \boldsymbol{\varepsilon}_s = \begin{bmatrix} \bar{u}_{x,z} + t\left(p_{x,z} + p_{z,x}\right) + t_{,z}p_x + \bar{u}_{z,x} \\ \bar{u}_{y,z} + t\left(p_{y,z} + p_{z,y}\right) + t_{,z}p_y + \bar{u}_{z,y} \end{bmatrix}; \ \varepsilon_{zz} = \left[\bar{u}_{z,z} + tp_{z,z} + t_{,z}p_z\right] \tag{14}$$

Replacing the displacement fields approximated by eq. (11) into the strain fields in eq. (14), the relations between the strains and nodal displacements $\mathbf{q}_e$ of the element in the local coordinate system can be obtained as follows

$$\boldsymbol{\varepsilon}_m = \sum_{I=1}^{4} \mathbf{B}_{mI}\mathbf{q}_{eI} \tag{15}$$

$$\boldsymbol{\varepsilon}_b = \sum_{I=1}^{4} \mathbf{B}_{bI}\mathbf{q}_{eI} \tag{16}$$

$$\boldsymbol{\varepsilon}_s = \sum_{I=1}^{4} \mathbf{B}_{sI}\mathbf{q}_{eI} \tag{17}$$

$$\varepsilon_{zz} = \sum_{I=1}^{4} \mathbf{B}_{zI}\mathbf{q}_{eI} \tag{18}$$

in which, $\mathbf{q}_{eI} = \left[\bar{u}_{xI} \ \bar{u}_{yI} \ \bar{u}_{zI} \ p_{xI} \ p_{yI} \ p_{zI}\right]^T$ and $\mathbf{B}_{mI}$, $\mathbf{B}_{bI}$, $\mathbf{B}_{sI}$, and $\mathbf{B}_{zI}$ are the standard gradient matrices and will be modified in the following discussion.
To establish formulations for locking removal and separate bending strain interpolation, the strain fields in the parent coordinate system can be expressed by ones in the local coordinate system as

$$\left[\varepsilon_{rr} \ \varepsilon_{ss} \ \varepsilon_{tt} \ \gamma_{rs} \ \gamma_{rt} \ \gamma_{st}\right]^T = \mathbf{T}^{-1}\left[\varepsilon_{xx} \ \varepsilon_{yy} \ \varepsilon_{zz} \ \gamma_{xy} \ \gamma_{xz} \ \gamma_{yz}\right]^T \tag{19}$$

with

$$\mathbf{T}=\begin{bmatrix} I_{11}^2 & I_{21}^2 & I_{31}^2 & I_{11}I_{21} & I_{11}I_{31} & I_{21}I_{31} \\ I_{12}^2 & I_{22}^2 & I_{32}^2 & I_{11}I_{22} & I_{12}I_{32} & I_{22}I_{32} \\ I_{13}^2 & I_{23}^2 & I_{33}^2 & I_{13}I_{23} & I_{13}I_{33} & I_{23}I_{33} \\ 2I_{11}I_{12} & 2I_{21}I_{22} & 2I_{31}I_{32} & I_{12}I_{21}+I_{11}I_{22} & I_{12}I_{31}+I_{11}I_{32} & I_{22}I_{31}+I_{21}I_{32} \\ 2I_{11}I_{13} & 2I_{21}I_{23} & 2I_{31}I_{33} & I_{23}I_{11}+I_{21}I_{13} & I_{13}I_{13}+I_{11}I_{33} & I_{23}I_{31}+I_{21}I_{33} \\ 2I_{11}I_{13} & 2I_{11}I_{13} & 2I_{11}I_{13} & I_{23}I_{12}+I_{22}I_{13} & I_{13}I_{32}+I_{12}I_{33} & I_{23}I_{32}+I_{22}I_{33} \end{bmatrix} \tag{20}$$

wherein, I_{ij} is the component located at row i and column j of the inverse of the Jacobian matrix **J** determined by

$$\mathbf{J}=\begin{bmatrix} \mathbf{R}_x^T\mathbf{X}_{,r} & \mathbf{R}_y^T\mathbf{X}_{,r} & \mathbf{R}_z^T\mathbf{X}_{,r} \\ \mathbf{R}_x^T\mathbf{X}_{,s} & \mathbf{R}_y^T\mathbf{X}_{,s} & \mathbf{R}_z^T\mathbf{X}_{,s} \\ \mathbf{R}_x^T\mathbf{X}_{,t} & \mathbf{R}_y^T\mathbf{X}_{,t} & \mathbf{R}_z^T\mathbf{X}_{,t} \end{bmatrix} \tag{21}$$

Then, the gradient matrices $\mathbf{B}_{sI}$ and $\mathbf{B}_{zI}$ in eq. (17) and eq. (18) can explicitly rewritten by

$$\mathbf{B}_{sI}=\begin{bmatrix} I_{13}I_{13}+I_{11}I_{33} & I_{23}I_{31}+I_{21}I_{33} \\ I_{13}I_{32}+I_{12}I_{33} & I_{23}I_{32}+I_{22}I_{33} \end{bmatrix}\begin{bmatrix} 0 & 0 & N_{I,r} & N_I & 0 & 0 \\ 0 & 0 & N_{I,s} & 0 & N_I & 0 \end{bmatrix}\begin{bmatrix} \mathbf{J} & \mathbf{J} \\ \mathbf{J} & \mathbf{J} \end{bmatrix} \tag{22}$$

$$\mathbf{B}_{zI}=I_{33}^2\begin{bmatrix} 0 & 0 & 0 & 0 & 0 & N_I \end{bmatrix}\begin{bmatrix} \mathbf{0}_{3x3} & \mathbf{0}_{3x3} \\ \mathbf{0}_{3x3} & \mathbf{J} \end{bmatrix} \tag{23}$$

To attenuate the shear-locking phenomenon when the thickness of plates or shells becomes thin, the transverse shear strains are separately interpolated and connected to the displacement approximation given in eq. (11) through the tying points. This interpolation, namely the MITC4 technique, was introduced by Bathe and Dvorkin [21] as follows

$$\begin{aligned} \tilde{\gamma}_{rt} &= 0.5(1-s)\gamma_{rt}^{(A_1)}+0.5(1+s)\gamma_{rt}^{(A_3)} \\ \tilde{\gamma}_{st} &= 0.5(1-r)\gamma_{st}^{(A_2)}+0.5(1+r)\gamma_{st}^{(A_4)} \end{aligned} \tag{24}$$

in which, $\gamma_{rt}^{(A_1)},\gamma_{st}^{(A_2)},\gamma_{rt}^{(A_3)}$, and $\gamma_{st}^{(A_4)}$ are respectively the values of the transverse shear strains determined by the displacement approximation in eq. (11) and the transverse shear strains in eq. (17) at points A_1(0,-1,0), A_2(1,0,0), A_3(0,1,0), and A_4(-1,0,0) in the parent coordinate system.

Transforming from the parent coordinate system to the local one, the transverse shear strains according to the MITC4 technique can be expressed in the nodal displacements by

$$\hat{\boldsymbol{\varepsilon}}_s=\sum_{I=1}^{4}\hat{\mathbf{B}}_{sI}\mathbf{q}_{eI} \tag{25}$$

Due to distorted meshes in largely curved shells, there is parasitic transverse normal strain due to the trapezoidal shape in the thickness direction of elements. This trapezoidal-locking phenomenon can be overcome by employing the following interpolation of the transverse normal strain [5]

$$\hat{\varepsilon}_{tt}=0.25(1-r)(1-s)\varepsilon_{tt}^{(B_1)}+0.25(1+r)(1-s)\varepsilon_{tt}^{(B_2)}+0.25(1+r)(1+s)\varepsilon_{tt}^{(B_3)}+0.25(1-r)(1+s)\varepsilon_{tt}^{(B_4)} \tag{26}$$

here, $\varepsilon_{tt}^{(B_1)},\varepsilon_{tt}^{(B_2)},\varepsilon_{tt}^{(B_3)}$, and $\varepsilon_{tt}^{(B_4)}$ are respectively the values of the transverse normal strains in eq. (18) evaluated at points B_1(-1,-1,0), B_2(1,-1,0), B_3(1,1,0), and B_4(-1,1,0) using the displacement approximation given in eq. (11).

Similarly, the transverse normal strain in eq. (26) is transformed into the one in the local coordinate system which relates to the nodal displacements as follows

$$\hat{\varepsilon}_{zz}=\sum_{I=1}^{4}\hat{\mathbf{B}}_{zI}\mathbf{q}_{eI} \tag{27}$$

In this study, the bending strains $\boldsymbol{\varepsilon}_b$ in eq. (14) are also interpolated again based on the technique suggested by Choi and Paik [10]. According to this technique, the bending strains in the parent coordinate system $\left[\varepsilon_{rr}^b\ \varepsilon_{ss}^b\ \gamma_{rs}^b\right]^T$ are interpolated through the values of the bending strains directly derived from the displacement approximation at points A_1(0,-1,0), A_2(1,0,0), A_3(0,1,0), and A_4(-1,0,0)

$$\begin{aligned} \hat{\varepsilon}_{rr}^b &= \frac{1}{2}\left(\varepsilon_{rr}^{b(A_1)}+\varepsilon_{rr}^{b(A_3)}\right)+\frac{1}{2}\left(\varepsilon_{rr}^{b(A_1)}+\varepsilon_{rr}^{b(A_3)}\right)s \\ \hat{\varepsilon}_{ss}^b &= \frac{1}{2}\left(\varepsilon_{ss}^{b(A_1)}+\varepsilon_{ss}^{b(A_3)}\right)+\frac{1}{2}\left(\varepsilon_{ss}^{b(A_1)}+\varepsilon_{ss}^{b(A_3)}\right)r \\ \hat{\gamma}_{rs}^b &= \frac{1}{4}\left(\gamma_{rs}^{b(A_1)}+\gamma_{rs}^{b(A_2)}+\gamma_{rs}^{b(A_3)}+\gamma_{rs}^{b(A_4)}\right) \end{aligned} \tag{28}$$

Substituting the bending strains in eq. (16) transformed to the parent coordinate system into eq. (28), the approximated bending strains in eq. (28) in the local coordinate system can be formulated the relation to the nodal displacements as

$$\hat{\boldsymbol{\varepsilon}}_b=\sum_{I=1}^{4}\hat{\mathbf{B}}_{bI}\mathbf{q}_{eI} \tag{29}$$

To improve the effectiveness of the proposed element, the membrane strains are smoothed on cell-based domains [12,22]. To this cell-based smoothed technique, the membrane strains are averaged by

$$\hat{\boldsymbol{\varepsilon}}_m = \frac{1}{A_{cs}}\int_{\Omega_{cs}} \boldsymbol{\varepsilon}_m d\Omega \tag{30}$$

in which, A_{cs} is the areas of the smoothing domains Ω_{cs} defined by 1, 2, 3 or 4 sub-cells of an element as depicted in **Fig. 2**.

From eq. (14) and eq. (15), the smoothed membrane strains given in eq. (30) are expressed

$$\hat{\boldsymbol{\varepsilon}}_m = \frac{1}{A_{cs}}\int_{\Omega_{cs}} \sum_{I=1}^{4} \begin{bmatrix} N_{I,x} & 0 & 0 & 0 & 0 & 0 \\ 0 & N_{I,y} & 0 & 0 & 0 & 0 \\ N_{I,y} & N_{I,x} & 0 & 0 & 0 & 0 \end{bmatrix} \mathbf{q}_{eI} d\Omega = \frac{1}{A_{cs}} \sum_{I=1}^{4} \begin{bmatrix} \int_{\Omega_{cs}} N_{I,x} d\Omega & 0 & 0 & 0 & 0 & 0 \\ 0 & \int_{\Omega_{cs}} N_{I,y} d\Omega & 0 & 0 & 0 & 0 \\ \int_{\Omega_{cs}} N_{I,y} d\Omega & \int_{\Omega_{cs}} N_{I,x} d\Omega & 0 & 0 & 0 & 0 \end{bmatrix} \mathbf{q}_{eI} \tag{31}$$

Applying the divergence theorem to the integrations of the derivatives of the shape functions, eq. (31) can be rewritten by

$$\hat{\boldsymbol{\varepsilon}}_m = \sum_{I=1}^{4} \underbrace{\left(\frac{1}{A_{cs}} \begin{bmatrix} \int_{\Gamma_{cs}} N_I n_x d\Gamma & 0 & 0 & 0 & 0 & 0 \\ 0 & \int_{\Gamma_{cs}} N_I n_y d\Gamma & 0 & 0 & 0 & 0 \\ \int_{\Gamma_{cs}} N_I n_y d\Gamma & \int_{\Gamma_{cs}} N_I n_x d\Gamma & 0 & 0 & 0 & 0 \end{bmatrix} \right)}_{\hat{\mathbf{B}}_{mI}} \mathbf{q}_{eI} = \sum_{I=1}^{4} \hat{\mathbf{B}}_{mI} \mathbf{q}_{eI} \tag{32}$$

here, Γ_{cs} is the boundary of the smoothing domains Ω_{cs}; n_x and n_y are the direction cosines of the unit vector normal to Γ_{cs}.

The gradient matrix $\hat{\mathbf{B}}_{mI}$ in eq. (32) is computed by using one Gaussian quadrature point on each edge of the boundary Γ_{cs}. The values of the shape functions at the Gaussian quadrature points $\mathbf{r}_{qp}$ for the cases of 1, 2, 3 or 4 smoothing sub-cells are provided in Fig. 2. The gradient matrix $\hat{\mathbf{B}}_{mI}$ is therefore determined

$$\hat{\mathbf{B}}_{mI} = \frac{1}{A_{cs}} \sum_{ed=1}^{4} \begin{bmatrix} N_I(\mathbf{r}_{qp}) n_x & 0 & 0 & 0 & 0 & 0 \\ 0 & N_I(\mathbf{r}_{qp}) n_y & 0 & 0 & 0 & 0 \\ N_I(\mathbf{r}_{qp}) n_y & N_I(\mathbf{r}_{qp}) n_x & 0 & 0 & 0 & 0 \end{bmatrix} l_{ed} \tag{33}$$

where, l_{ed} is the length of each edge of the smoothing sub-cells.

From eq. (25), eq. (27), eq. (29), and eq. (32), the strain energy of the proposed CSn-S8 element, or CS1-S8, CS2-S8, CS3-S8 and CS4-S8 for 1, 2, 3 and 4 smoothing sub-cells used, in the scope of linear elasticity is [6]

$$\hat{\Pi}^e = \frac{1}{2}\int_{-1}^{1}\int_{-1}^{1}\int_{-1}^{1} \left\{ \left(\hat{\boldsymbol{\varepsilon}}_m + t\hat{\boldsymbol{\varepsilon}}_b\right)^T \mathbf{C}_{mb} \left(\hat{\boldsymbol{\varepsilon}}_m + t\hat{\boldsymbol{\varepsilon}}_b\right) + \hat{\varepsilon}_{zz} C_z \hat{\varepsilon}_{zz} + \hat{\boldsymbol{\varepsilon}}_s^T \mathbf{C}_s \hat{\boldsymbol{\varepsilon}}_s \right\} |\mathbf{J}| dr ds dt \tag{34}$$

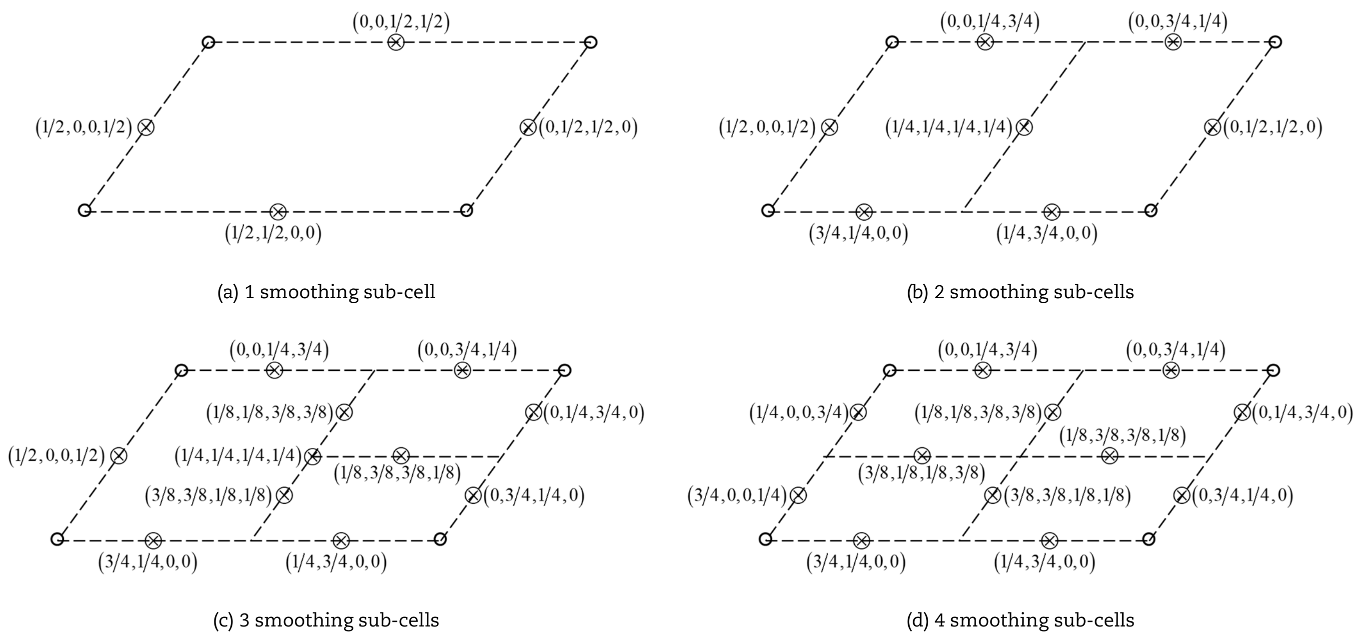

Fig. 2. Division of an element into 1, 2, 3, or 4 smoothing sub-cells and values of the shape functions (N_1, N_2, N_3, N_4) at the quadrature points.

wherein,

$$\mathbf{C}_{mb} = \frac{E}{1-\nu^2}\begin{bmatrix} 1 & \nu & 0 \\ \nu & 1 & 0 \\ 0 & 0 & (1-\nu)/2 \end{bmatrix};\ C_z = E;\ \mathbf{C}_s = \frac{E}{2(1+\nu)}\begin{bmatrix} 1 & 0 \\ 0 & 1 \end{bmatrix} \tag{35}$$

and E is the Young's modulus and ν is the Poisson's ratio.

Integrating eq. (34) through the thickness, the strain energy of the element can be rewritten

$$\hat{\Pi}^e = \frac{1}{2}\int_{-1}^{1}\int_{-1}^{1}\left\{\hat{\boldsymbol{\varepsilon}}_m^T \mathbf{D}_m \hat{\boldsymbol{\varepsilon}}_m + \hat{\boldsymbol{\varepsilon}}_b^T \mathbf{D}_b \hat{\boldsymbol{\varepsilon}}_b + \hat{\varepsilon}_{zz} D_z \hat{\varepsilon}_{zz} + \hat{\boldsymbol{\varepsilon}}_s^T \mathbf{D}_s \hat{\boldsymbol{\varepsilon}}_s\right\}|\mathbf{J}|drds \tag{36}$$

in which,

$$\mathbf{D}_m = \int_{-1}^{1}\mathbf{C}_{mb}dt;\ \mathbf{D}_b = \int_{-1}^{1}t^2\mathbf{C}_{mb}dt;\ D_z = \int_{-1}^{1}C_z dt;\ \mathbf{D}_s = \int_{-1}^{1}\mathbf{C}_s dt \tag{37}$$

From the strain energy and following the standard procedure of the FEM, the stiffness matrix of the CSn-S8 element can be obtained

$$\hat{\mathbf{k}}^e = \hat{\mathbf{k}}_m^e + \hat{\mathbf{k}}_b^e + \hat{\mathbf{k}}_z^e + \hat{\mathbf{k}}_s^e \tag{38}$$

wherein,

$$\hat{\mathbf{k}}_m^e = \sum_{sc=1}^{N_{sc}}\left(\sum_{I=1}^{4}\hat{\mathbf{B}}_{mI}^T \mathbf{D}_m \hat{\mathbf{B}}_{mI}\right)A_{sc};\ \hat{\mathbf{k}}_b^e = \int_{-1}^{-1}\int_{-1}^{-1}\left(\sum_{I=1}^{4}\hat{\mathbf{B}}_{bI}^T \mathbf{D}_b \hat{\mathbf{B}}_{bI}\right)|\mathbf{J}|drds;\ \hat{\mathbf{k}}_z^e = \int_{-1}^{-1}\int_{-1}^{-1}\left(\sum_{I=1}^{4}\hat{\mathbf{B}}_{zI}^T D_z \hat{\mathbf{B}}_{zI}\right)|\mathbf{J}|drds;\ \hat{\mathbf{k}}_s^e = \int_{-1}^{-1}\int_{-1}^{-1}\left(\sum_{I=1}^{4}\hat{\mathbf{B}}_{sI}^T \mathbf{D}_s \hat{\mathbf{B}}_{sI}\right)|\mathbf{J}|drds; \tag{39}$$

with N_{sc} = 1, 2, 3 or 4 smoothing sub-cells.

3. Numerical Verifications

In the following numerical examples, the presented elements were used to determine static displacements of some benchmark plates and shells. The proposed elements were implemented by using MATLAB software on a laptop with an i7-8550U CPU. To investigate the accuracy and convergence, the plates and shells were discretized by only one element through the thickness and $N_X \times N_Y$ elements on the middle surface, in which N_X and N_Y were respectively the number of elements on the X- and Y-directions. The numerical results given by the presented elements were compared with the flat shell elements employing the MITC3+ [23] or MITC4 [21] techniques, the QUAD4 flat shell element with selective reduced order integration [24], the Xshell41 4-node assumed strain quasi-conforming flat shell element with drilling rotation [25], the Xsolid83 or Xsolid85 resultant 8-node solid shell elements [6], and the RH8s-4 smoothed resultant 8-node solid shell element [19].

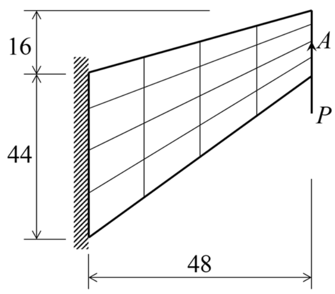

Fig. 3. Geometry, boundary, load, and 4×4 mesh of the Cook's membrane plate.

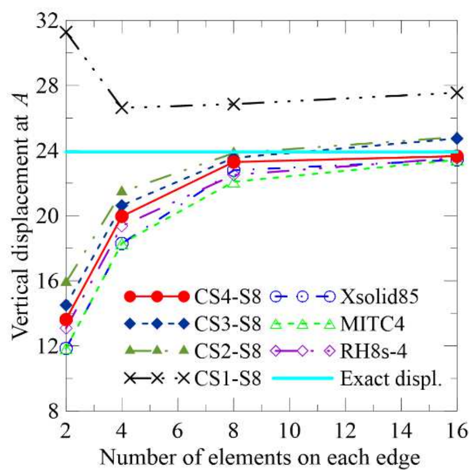

Fig. 4. Vertical displacement at A given by the presented elements and others.

Table 1. Normalized deflection at the center of the clamped square plate with $h/L = 10^{-3}$.

Elements	$N_x \times N_y$				% relative errors	CPU time (seconds)
	4×4	8×8	12×12	16×16		16×16
MITC3+ [23]	0.1235	0.1259	0.1263	0.1264	0.2368	3.03
MITC4 [21]	0.1211	0.1251	0.1259	0.1262	0.3946	1.16
CS1-S8	0.1256	0.1263	0.1264	0.1265	0.1973	14.27
CS2-S8	0.1256	0.1263	0.1264	0.1265	0.1973	14.66
CS3-S8	0.1256	0.1263	0.1264	0.1265	0.1973	15.13
CS4-S8	0.1256	0.1263	0.1264	0.1265	0.1973	15.64

Table 2. Normalized deflection at the center of the clamped square plate with h/L from 10^{-3} to 10^{-8}.

Elements	h/L					
	10^{-3}	10^{-4}	10^{-5}	10^{-6}	10^{-7}	10^{-8}
MITC3+ [23]	0.1264	0.1263	0.1184	0.0179	0.0005	0.0002
MITC4 [21]	0.1262	0.1266	0.1268	0.1155	0.0183	0.0001
CSn-S8	0.1265	0.1264	0.1256	0.1282	0.1193	0.1074

3.1 Cook's Membrane Plate

Consider a cantilever plate with dimensions and load proposed by Cook [26] as shown in **Fig. 3**. The plate's thickness is $h = 1$ and the material's properties are $E = 1$ and $\nu = 1/3$. With the concentrated load $P = 1$ applied at the middle point A of the free edge, the exact vertical displacement at A is 23.91.

To evaluate the membrane behaviors of the presented element, the plate is discretized by different meshes of $N_X = N_Y = 2$, 4, 8, and 16 elements. The vertical displacement at A given by the presented elements and others are illustrated in **Fig. 4**. The results given by the proposed CSn-S8 elements, except for the CS1-S8 element, approached the exact displacement at A according to the low-bound criteria of the standard FEM when the mesh refinements increased. However, the CS2-S8 and CS3-S8 elements predict slightly larger results than the exact displacement. It means the lower the number of sub-cells that the cell-based membrane strain smoothing technique used, the softer membrane stiffness the proposed elements had. In this example of the pure membrane behavior, **Fig. 4** suggests that the presented element using 4 smoothing sub-cells (CS4-S8) could obtain the best accuracy. As compared with the exact displacement, the CS4-S8 element provided more accurate results than those obtained by the MITC4 flat shell element and other 8-node solid shell elements like Xsolid85 and RH8s-4.

3.2 Square Bending Plate

A square plate is clamped all edges and subjected to uniformly distributed load $p = 1$ as shown in **Fig. 5**. The plate has the length $L = 10$, the thickness $h = 0.01$, and material properties of $E = 1092000$ and $\nu = 0.3$. According to the analytical method [27], the normalized deflection at the plate's center is 0.1267.

The plate is meshed by $N_X \times N_Y$ = 4×4, 8×8, 12×12, and 16×16 elements. Because the plate only bends, the membrane strain smoothing technique does not influence the results as listed in **Table 1**. The proposed element well converged to the analytical solution with the relative error below 0.2% for the mesh of 16×16 elements. The CSn-S8 element predicted the central deflection more accurately than those given by the MITC3+ and MITC4 flat shell elements. This is because of the benefit of the bending strain approximation used in the presented element. **Table 1** also shows the comparison of the computational time consumed by the CSn-S8, MITC4 and MITC3+ elements for the mesh of 16×16 elements. The number of sub-cells used in the proposed elements slightly influenced the CPU time. Because of twice the number of the degrees of freedom, the CSn-S8 solid shell elements consumed more computational time than those of the MITC3+ and MITC4 plate elements.

To assess the ability of the shear-locking removal of the suggested element, the thickness-to-length ratio of the plate was reduced from 10^{-3} to 10^{-8}. As shown in **Table 2**, the CSn-S8 element could overcome the shear-locking phenomenon until $h/L = 10^{-8}$ while the shear locking occurred at $h/L = 10^{-5}$ for the MITC3+ element and $h/L = 10^{-6}$ for the MITC4 element.

3.3 Rectangular Bending Plate

Clamped plates under concentrated load $P = 4\times10^4$ at the center in **Fig. 6** were considered in this example. The plate's thickness is $h = 0.01$. The material properties of the plate are $E = 1.7472\times10^7$ and $\nu = 0.3$. The reference deflections at the center are respectively 5.6×10^{-6} and 7.23×10^{-6} for the plates with dimensions $L\times L = 2\times2$ and $L\times5L = 2\times10$ [6].

Due to symmetry, a quarter of the plate is modeled by meshes of $N_X \times N_Y$ = 2×2, 4×4, 6×6, 8×8 and 16×16 elements. In comparison with the reference deflections, the graphs of element size versus relative error of the central deflections in the logarithm scale given by the presented element and others are demonstrated in **Fig. 7**. The convergence rate of the CSn-S8 was the same as those of other solid and flat shell elements for both square and rectangular plates. The presented element obtained better results than those of Xsolid83 and Xsolid85 solid shell elements. For the mesh of 8×8 elements, the CSn-Q8 solid shell elements gave worse results than those of the Xshell41 and QUAD4 flat shell elements. However, when using the fine mesh of 16×16 elements, the CSn-Q8 elements provided better results with about 0.1% and 1% relative errors for square and rectangular plates, respectively.

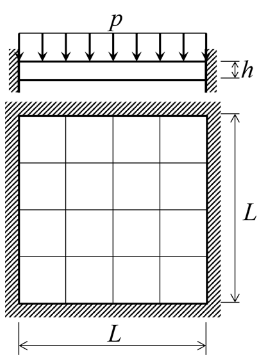

Fig. 5. Geometry, clamped boundary, uniformly distributed load, and 4×4 mesh of the square bending plate.

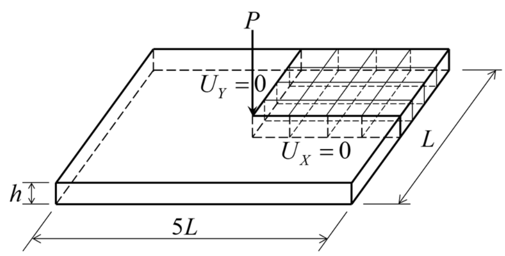

Fig. 6. Geometry, clamped boundary, concentrated load, and 4×4 mesh of the rectangular bending plate.

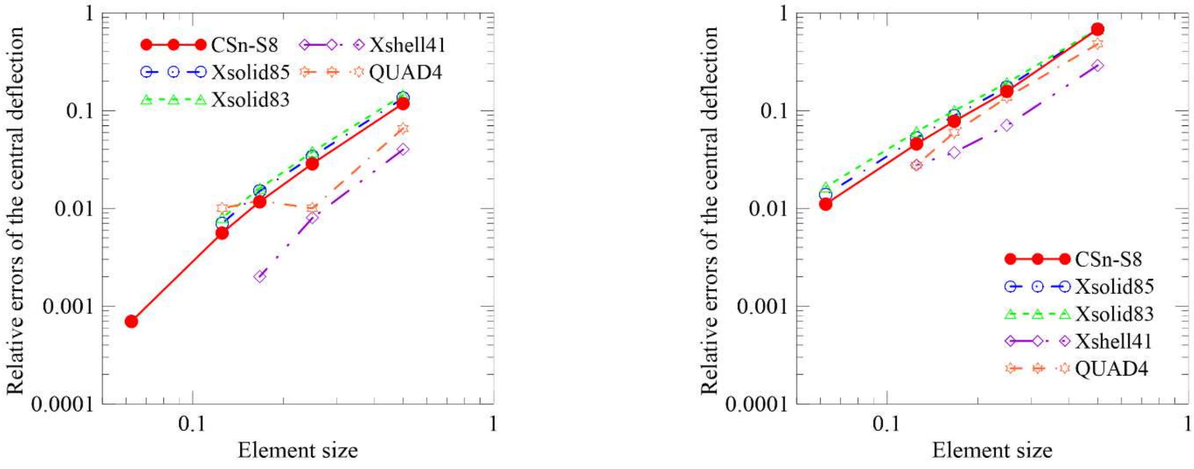

(a) Square plate ($a \times a$)

(b) Rectangular plate ($a \times b$)

Fig. 7. Convergence rate and accuracy of the central deflection of clamped square and rectangular plates under concentrated load.

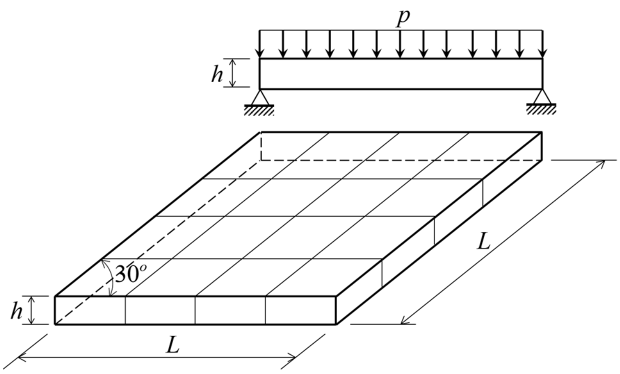

Fig. 8. Geometry, clamped boundary, uniformly distributed load, and 4×4 mesh of the rhombic bending plate.

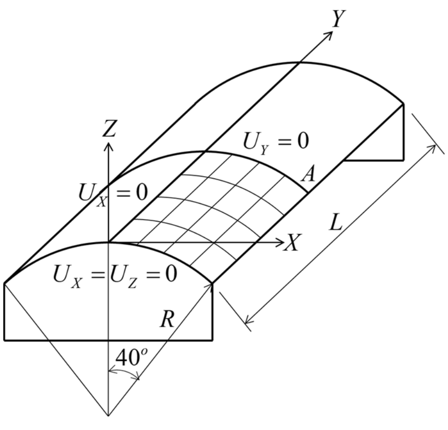

Fig. 9. Geometry, boundary, and 4×4 mesh of the Scordellis-Lo roof.

Because the number of elements in the meshes for both square and rectangular plates are identical, the meshes used to model the rectangular plate are rectangular elements and coarser than those of the square plate. As a result, all elements predicted the central deflections of the square plate more accurately than those of the rectangular one.

3.4 Rhombic Bending Plate

A Morley's rhombic plate given in **Fig. 6** has the length $L = 100$, thickness $h = 1$, and acute angle $\theta = 30^o$ [28]. The plate is simply supported on all edges and subjected to uniformly distributed load $p = 1$. The plate is made of material with $E = 10\times10^6$ and $\nu = 0.3$. The reference deflection at the plate's center is 0.04455.

The rhombic plate is discretized by meshes of $N_X = N_Y = 8$, 16, and 20 elements. Due to the rhombic shape of the plate, the meshes include 8-node solid-shell elements with very acute angles and strongly influence the numerical results. The central deflections of the rhombic plate predicted by the presented elements and other finite elements are listed in **Table 3** for various meshes. As shown in **Table 3**, the proposed element could obtain very good deflection with the smallest relative error as compared with the Xsolid85 solid, MITC3+ and MITC4 flat shell elements. Particularly, when using the mesh of 20×20 elements, the CS4-S8 element could achieve the reference deflection with the relative error of 0.1122% while the relative errors predicted by the other elements were above 5%. The enhancement of the CSn-S8 element indicated the effectiveness of the proposed bending approximation.

Table 3. Central deflection of the simply supported rhombic plate under uniformly distributed load.

Elements	$N_x \times N_y$			% relative errors
	8×8	16×16	20×20	
Xsolid85 [6]	0.0388	0.0413	0.0422	5.2076
MITC3+ [23]	0.0291	0.0330	0.0369	17.2615
MITC4 [21]	0.0357	0.0384	0.0410	7.9910
CSn-S8	0.0428	0.0435	0.0445	0.1122

Table 4. Vertical displacement at point *A* of the Scordellis-Lo roof.

Elements	$N_x \times N_y$			% relative errors
	4×4	8×8	16×16	
MITC3+ [23]	0.2304	0.2769	0.3066	1.3889
MITC4 [21]	0.2851	0.2958	0.3049	0.8267
Xsolid85 [6]	0.2903	0.2976	0.3021	0.0992
RH8s-4 [19]	0.3293	0.3148	0.3088	2.1164
CS1-S8	0.3587	0.3185	0.3080	1.8519
CS2-S8	0.3279	0.3105	0.3060	1.1905
CS3-S8	0.3143	0.3066	0.3050	0.8598
CS4-S8	0.3020	0.3027	0.3040	0.5291

3.5 Scordellis-Lo Roof Shell

Consider a Scordellis-Lo roof shell subjected to the self-weight p = 90. The roof's dimensions are the length L = 50, radius R = 25 and thickness h = 0.25 as illustrated in **Fig. 9**. The Young's modulus and Poisson's ratio of the roof's material are respectively $E = 4.32\times10^8$ and $\nu = 0$. The ends of the roof are rigid diaphragms and the other edges are free. The reference vertical displacement of point *A* located at the middle free edge is 0.3024 [29].

With a quarter of the roof simulated because of the symmetry, the displacement constraints are described in **Fig. 9**. The roof is discretized by 4×4, 8×8, and 16×16 elements. The vertical displacements at point *A* given by the presented elements using 1, 2, 3, and 4 sub-cells for smoothing the membrane strains are listed in **Table 4**. Among these presented elements, the CS4-S8 element predicted the smallest relative error as compared with the reference results. The CS4-S8 element also gave more accurate displacement than MITC3+, MITC4 flat shell elements and RH8s-4 smoothed solid shell element. Despite being not as good as the Xsolid85 element in this example, the suggested element could obtain the acceptable result by employing the coarse mesh of 4×4 elements as demonstrated in **Fig. 10**.

3.6 Pinched Cylinder with End Diaphragm

A cylindrical shell of the radius R = 300, thickness h = 3, and L = 600 is applied to two concentrated loads P =1 as shown in **Fig. 11** and its two ends are rigid diaphragms. The material properties of the pinched cylinder are $E = 3\times10^6$ and ν = 0.3. The vertical displacement at the load's position (point *A*) is 1.8248×10^{-5} [30].

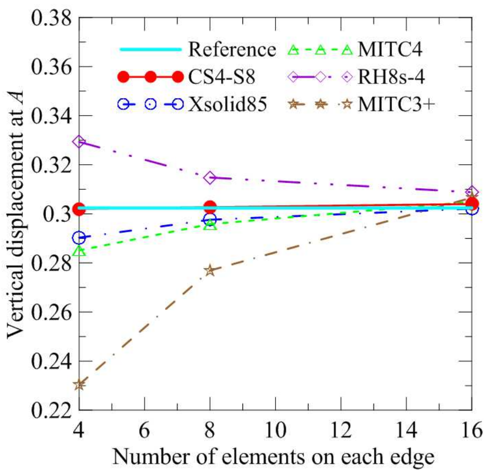

Fig. 10. Convergence and accuracy of the vertical displacement at point *A* of the Scordellis-Lo roof.

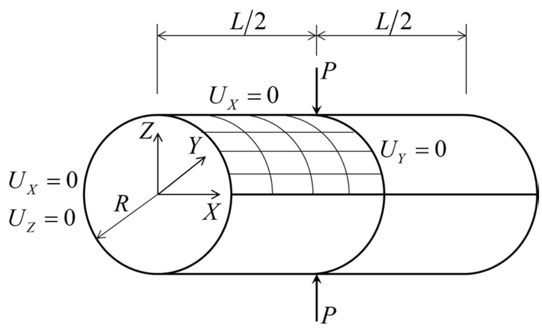

Fig. 11. Geometry, boundary, concentrate load, and 2×2 mesh of the pinched cylinder.

Table 5. Vertical displacement at point A of the pinched cylinder.

Elements	$N_x \times N_y$			% relative errors	CPU time (minutes)
	8×8	16×16	32×32		32×32
MITC3+ [23]	1.4123×10^{-5}	1.7158×10^{-5}	1.7602×10^{-5}	3.2857	9.00
MITC4 [21]	1.3559×10^{-5}	1.6944×10^{-5}	1.7450×10^{-5}	4.1209	3.81
Xsolid85 [6]	7.3904×10^{-6}	1.5292×10^{-5}	1.7810×10^{-5}	2.1429	-
RH8s-4 [19]	1.3832×10^{-5}	1.7044×10^{-5}	1.8066×10^{-5}	0.7363	-
CS1-S8	1.1009×10^{-5}	1.6968×10^{-5}	1.8063×10^{-5}	0.7527	4.15
CS2-S8	1.0702×10^{-5}	1.6866×10^{-5}	1.8051×10^{-5}	0.8187	4.17
CS3-S8	1.0637×10^{-5}	1.6844×10^{-5}	1.8033×10^{-5}	0.9176	4.20
CS4-S8	1.0579×10^{-5}	1.6822×10^{-5}	1.8028×10^{-5}	0.9451	4.24

Because of symmetry, one-eighth of the pinched cylinder is modeled by meshes of 8×8, 16×16, 32×32 elements. The vertical displacements at point A obtained by the suggested elements were compared with those given by other elements in **Table 5**. In this example, as compared with other CSn-S8 elements, the vertical displacement given by the CS1-S8 element was the largest because the CS1-S8 element had the softest membrane stiffness. However, the difference in the relative errors of the displacement between the CS1-S8 and CS4-S8 elements is not large, about 0.2%. **Table 5** also indicated that with the identical meshes of 32×32 elements and degrees of freedom, the computational time of the CSn-S8 solid shell elements was not much lower than that of the MITC4 flat shell elements. The MITC3+ elements wasted the most CPU time due to double the number of elements used. For the Xsolid85 and RH8s-4 elements, the CPU time was not presented because there is no information in the references.

As seen in **Fig. 12**, the presented elements and RH8s-4 had similar convergence and accuracy and performed more superior results than those of MITC3+, MITC4 and Xsolid85 shell elements.

3.7 Hemispherical Shell with 18° Hole

A hemispherical shell with 18° hole in **Fig. 13** was considered in this example. The hemispherical shell has the radius R = 10, thickness h = 0.04, Young's modulus $E = 6.825\times10^7$, and Poisson's ratio ν = 0.3. The hemispherical shell is subjected to concentrated loads P = 2 along X- and Y-directions at the equator as shown in **Fig. 13**. The top and bottom circular boundaries are free. The reference X-displacement at the position of the applied load, point A, is 0.094 [24].

A quarter of the hemispherical shell with symmetric boundaries given in **Fig. 13** is simulated by meshes of $N_x = N_Y$ = 4, 8, 16, 20, and 32. The X-displacement at the applied load's position provided by the proposed elements and other references are presented in **Table 6**. The results given by the mesh of 20×20 and 32×32 elements were remarkably close. This means that all elements could obtain convergence results when using the 32×32 mesh. The relative errors between the numerical displacements given by the elements and the reference value versus number of elements on each edge are depicted in **Fig. 14**. As compared with other reference elements, the CSn-S8 elements obtained less percentage of the relative errors than those computed by the flat or solid shell elements like MITC3+, MITC4, Xsolid85, and RH8s-4. The CS4-S8 element could determine the most accurate result.

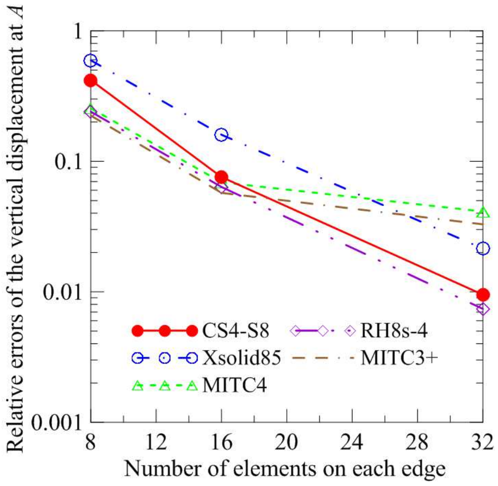

Fig. 12. Convergence and accuracy of the vertical displacement at point A of the pinched cylinder.

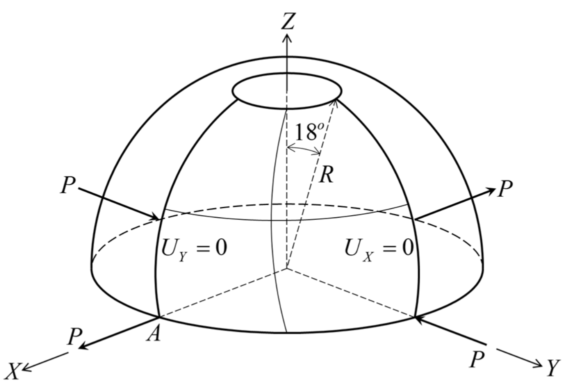

Fig. 13. Geometry, boundary, concentrate loads, and 2×2 mesh of the hemispherical shell with 18° hole.

Table 6. X-displacement at point A of the hemispherical shell with 18° hole.

Elements	$N_x \times N_y$					% relative errors
	4×4	8×8	16×16	20×20	32×32	
MITC3+ [23]	0.0992	0.0954	0.0935	0.0933	0.0934	1.0823
MITC4 [21]	0.0814	0.0913	0.0929	0.0930	0.0933	0.9740
Xsolid85 [6]	0.0995	0.0945	-	-	-	-
RH8s-4 [19]	0.0968	0.0937	0.0932	0.0932	0.0932	0.8658
CS1-S8	0.0819	0.0925	0.0926	0.0931	0.0927	0.3247
CS2-S8	0.0815	0.0922	0.0923	0.0929	0.0926	0.2165
CS3-S8	0.0812	0.0919	0.0921	0.0927	0.0926	0.2165
CS4-S8	0.0811	0.0918	0.0919	0.0926	0.0925	0.1082

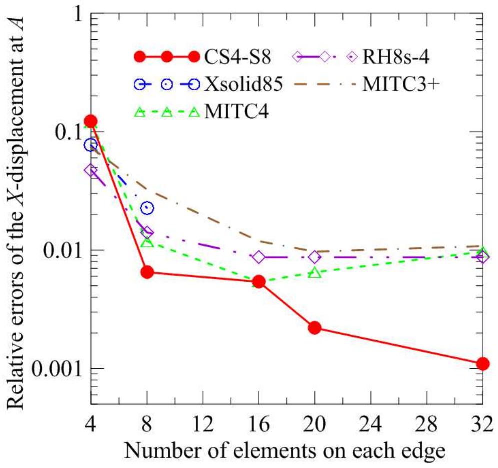

Fig. 14. Convergence and accuracy of the X-displacement at point A of the hemispherical shell with 18° hole.

4. Conclusion

A new 8-node solid-shell finite element has been presented. The proposed element is able to overcome the shear- and trapezoidal-locking phenomena, and could improve the prediction of the membrane and bending behaviors of plate and shell structures owing to the separate interpolation of the bending strains and the cell-based smoothing technique of the membrane strains. The presented CSn-S8 element was employed to statically analyze some typical plate and shell problems. Numerical results indicate that by using 4 sub-cells for smoothing the membrane strains, the presented element could obtain the excellent accuracy and convergence rate for membrane-dominated problems. The suggested approximation of the bending strains also showed the effectiveness of the CSn-Q8 element for analysis of bending-dominated plates and shells. The deflections given by the presented element were similar or better than those provided by many other flat shell or solid-shell finite elements previously published.

Author Contributions

T. Chau-Dinh planned the scheme, initiated the project, and suggested the implementation; N. Le-Tran conducted the programming and computed the numerical results. The manuscript was written through the contribution of all authors. All authors discussed the results, reviewed, and approved the final version of the manuscript.

Acknowledgments

This work belongs to the project grant No: T2019-73TĐ funded by Ho Chi Minh City University of Technology and Education, Vietnam.

Conflict of Interest

The authors declared no potential conflicts of interest with respect to the research, authorship and publication of this article.

Funding

The authors received financial support for the research and publication of this article.

Nomenclature

A_{cs}	Area of smoothing sub-cell
$\mathbf{B}_{mI}$, $\mathbf{B}_{bI}$, $\mathbf{B}_{sI}$, $\mathbf{B}_{zI}$,	Gradient matrices of membrane, bending, transvers shear and transverse normal strains
$\hat{\mathbf{B}}_{mI}$, $\hat{\mathbf{B}}_{bI}$, $\hat{\mathbf{B}}_{sI}$, $\hat{\mathbf{B}}_{zI}$	Gradient matrices of assumed membrane, bending, transverse shear and transverse normal strains
$\boldsymbol{\varepsilon}$	Strains in the local coordinate system
$\boldsymbol{\varepsilon}_m$, $\boldsymbol{\varepsilon}_b$, $\boldsymbol{\varepsilon}_s$, ε_{zz}	Membrane, bending, transvers shear and transverse normal strains in the local coordinate system
$\hat{\boldsymbol{\varepsilon}}$	Assumed strains in the local coordinate system
$\hat{\boldsymbol{\varepsilon}}_m$, $\hat{\boldsymbol{\varepsilon}}_b$, $\hat{\boldsymbol{\varepsilon}}_s$, $\hat{\varepsilon}_{zz}$	Assumed membrane, bending, transverse shear and transverse normal strains

E	Young's modulus
h	Thickness of plates or shells
$\mathbf{J}$	Jacobian matrix
$\hat{\mathbf{k}}$	Element stiffness matrix
$\hat{\mathbf{k}}_m$, $\hat{\mathbf{k}}_b$, $\hat{\mathbf{k}}_s$, $\hat{\mathbf{k}}_z$	Element stiffness matrices of membrane, bending, transverse shear and transverse normal parts
l_{ed}	Length of an edge of the smoothing sub-cells
L	Length of plates or shells
ν	Poisson's ratio
n_x, n_y	Direction cosine of the vector normal to the boundary of smoothing sub-cells
N_I	Shape functions
N_{sc}	Number of smoothing subcells
$\Omega_{\mathbf{cs}}$	Smoothing sub-cell
$\mathbf{p}$	Half of a displacement vector from bottom to top surfaces
$\mathbf{P}$	Half of a coordinate vector from bottom to top surfaces
$\mathbf{q}_{eI}$	Nodal displacements of node I
$\mathbf{r}_{qp}$	Gaussian quadrature point in the parent coordinate system
R	Radius of shells
$\mathbf{R}$	Transformation matrix from the local coordinate system to the global one
$\mathbf{T}$	Transformation matrix from the local coordinate system to the parent one
$\mathbf{u}$	Displacements in the local coordinates system
$\bar{\mathbf{u}}$	Displacements of the middle surface
$\mathbf{U}$	Displacements in the global coordinates system
$\mathbf{x}$	Point coordinates in the local coordinate system
$\mathbf{X}$	Point coordinates in the global coordinate system
$\bar{\mathbf{X}}$	Point coordinates of the middle surface

References

[1] Yang, H.T.Y., Saigal, S., Masud, A., Kapania, R.K., A Survey of Recent Shell Finite Elements, *International Journal for Numerical Methods in Engineering*, 47, 2000, 101–127.
[2] Kulikov, G.M., Plotnikova, S.V., A Family of ANS Four-node Exact Geometry Shell Elements in General Convected Curvilinear Coordinates, *International Journal for Numerical Methods in Engineering*, 83, 2010, 1376–1406.
[3] Andelfinger, U., Ramm, E., EAS-elements for Two-dimensional, Three-dimensional, Plate and Shell Structures and their Equivalence to HR-elements, *International Journal for Numerical Methods in Engineering,* 36, 1993, 1311–1337.
[4] Bathe, K.-J., Dvorkin, E.N., A Formulation of General Shell Elements—The Use of Mixed Interpolation of Tensorial Components, *International Journal for Numerical Methods in Engineering*, 22, 1986, 697–722.
[5] Sze, K.Y., Yao, L.Q., A Hybrid Stress ANS Solid-shell Element and its Generalization for Smart Structure Modelling. Part I—Solid-shell Element Formulation, *International Journal for Numerical Methods in Engineering*, 48, 2000, 545–564.
[6] Kim, K.D., Liu, G.Z., Han, S.C., A Resultant 8-node Solid-shell Element for Geometrically Nonlinear Analysis, *Computational Mechanics*, 35, 2004, 315–331.
[7] Sussman, T., Bathe, K.-J., 3D-shell Elements for Structures in Large Strains, *Computers & Structures*, 122, 2013, 2–12.
[8] Mostafa, M., An Improved Solid-shell Element based on ANS and EAS Concepts, *International Journal for Numerical Methods in Engineering*, 108, 2016, 1362–1380.
[9] Su, Z., Xue, P., Tang, Y., An Improved Solid-shell Element based on the Computational Condensation Technique, *International Journal of Mechanical Sciences*, 141, 2018, 236–244.
[10] Choi, C.-K., Paik, J.-G., An Efficient Four Node Degenerated Shell Element based on the Assumed Covariant Strain, *Structural Engineering and Mechanics, An International Journal*, 2, 1994, 17–34.
[11] Ko, Y., Lee, P.-S., A 6-node Triangular Solid-shell Element for Linear and Nonlinear Analysis, *International Journal for Numerical Methods in Engineering*, 111, 2017, 1203–1230.
[12] Liu, G.R., Nguyen-Thoi, T., *Smoothed Finite Element Methods*, CRC Press, 2010.
[13] Nguyen-Van, H., Nguyen-Hoai, N., Chau-Dinh, T., Tran-Cong, T., Large Deflection Analysis of Plates and Cylindrical Shells by an Efficient Four-node Flat Element with Mesh Distortions, *Acta Mechanica*, 226, 2015, 2693–2713.
[14] Cui, X., Liu, G.-R., Li, G., Zhang, G., Zheng, G., Analysis of Plates and Shells using an Edge-based Smoothed Finite Element Method, *Computational Mechanics*, 45, 2009, 141–156.
[15] Nguyen-Thoi, T., Phung-Van, P., Thai-Hoang, C., Nguyen-Xuan, H., A Cell-based Smoothed Discrete Shear Gap Method (CS-DSG3) using Triangular Elements for Static and Free Vibration Analyses of Shell Structures, *International Journal of Mechanical Sciences*, 74, 2013, 32–45.
[16] Shin, C.M., Lee, B.C., Development of a Strain-smoothed Three-node Triangular Flat Shell Element with Drilling Degrees of Freedom, *Finite Elements in Analysis and Design*, 86, 2014, 71–80.
[17] Nguyen-Thoi, T., Phung-Van, P., Luong-Van, H., Nguyen-Van, H., Nguyen-Xuan, H., A Cell-based Smoothed Three-node Mindlin Plate Element (CS-MIN3) for Static and Free Vibration Analyses of Plates, *Computational Mechanics*, 51, 2012, 65–81.
[18] Chau-Dinh, T., Nguyen-Duy, Q., Nguyen-Xuan, H., Improvement on MITC3 Plate Finite Element using Edge-based Strain Smoothing Enhancement for Plate Analysis, *Acta Mechanica*, 228, 2017, 2141–2163.
[19] Élie-Dit-Cosaque, X.J.-G., Gakwaya, A., Naceur, H., Smoothed Finite Element Method Implemented in a Resultant Eight-node Solid-shell Element for Geometrical Linear Analysis, *Computational Mechanics*, 55, 2015, 105–126.
[20] Leonetti, L., Nguyen-Xuan, H., A Mixed Edge-based Smoothed Solid-shell Finite Element Method (MES-FEM) for Laminated Shell Structures, *Composite Structures*, 208, 2019, 168–179.
[21] Bathe, K.-J., Dvorkin, E.N., A Four-node Plate Bending Element based on Mindlin/Reissner Plate Theory and a Mixed Interpolation, *International Journal for Numerical Methods in Engineering*, 21, 1985, 367–383.
[22] Nguyen-Thanh, N., Rabczuk, T., Nguyen-Xuan, H., Bordas, S.P.A., A Smoothed Finite Element Method for Shell Analysis, *Computer Methods in Applied Mechanics and Engineering*, 198, 2008, 165–177.
[23] Lee, Y., Lee, P.-S., Bathe, K.-J., The MITC3+ Shell Element and its Performance, *Computers & Structures*, 138, 2014, 12–23.
[24] Macneal, R.H., Harder, R.L., A Proposed Standard Set of Problems to Test Finite Element Accuracy, *Finite Elements in Analysis and Design*, 1, 1985, 3–20.
[25] Kim, K.D., Lomboy, G.R., Voyiadjis, G.Z., A 4-node Assumed Strain Quasi-conforming Shell Element with 6 Degrees of Freedom, *International Journal for Numerical Methods in Engineering*, 58, 2003, 2177–2200.

[26] Cook, R.D., Improved Two-dimensional Finite Element, *Journal of the Structural Division*, 100, 1974, 1851–1863.
[27] Taylor, R.L., Auricchio, F., Linked Interpolation for Reissner-Mindlin Plate Elements: Part II—A Simple Triangle, *International Journal for Numerical Methods in Engineering*, 36, 1993, 3057–3066.
[28] Morley, L.S.D., *Skew Plates and Structures*, Pergamon Press, Oxford, 1963.
[29] Scordellis, A.C., Lo, K.S., Computer Analysis of Cylindrical Shells, *Journal of the American Concrete Institute*, 61, 1964, 539–561.
[30] Fluge, W., *Stress in shells*, Berlin: Springer, 1960.

ORCID iD

Thanh Chau-Dinh https://orcid.org/0000-0002-7289-2904
Nhat Le-Tran https://orcid.org/0000-0002-0201-6693

How to cite this article: Thanh C.-D., Nhat L.-T. An 8-Node Solid-Shell Finite Element based on Assumed Bending Strains and Cell-Based Smoothed Membrane Strains for Static Analysis of Plates and Shells, *J. Appl. Comput. Mech.*, 6(SI), 2020, 1335–1347. https://doi.org/10.22055/JACM.2020.34192.2353